Check for updates

ARTICLE

MafG/MYH9-LCN2 axis promotes liver fibrosis through inhibiting ferroptosis of hepatic stellate cells

Yalan Deng[1,2], Liqing Lu[2,3], Dandan Zhu[2], Huajun Zhang[1,2], Ying Fu[2], Yuying Tan[2], Xuemei Tan[4], Ming Guo[2], Ye Zhang[2], Heping Yang[5], Bing Yang[5], Ting Liu[6✉] and Yongheng Chen[2✉]

Hepatic stellate cells (HSCs) secrete extracellular matrix for collagen deposition, contributing to liver fibrosis. Ferroptosis is a novel type of programmed cell death induced by iron overload-dependent lipid peroxidation. Regulation of ferroptosis in hepatic stellate cells (HSCs) may have therapeutic potential for liver fibrosis. Here, we found that Maf bZIP transcription factor G (MafG) was upregulated in human and murine liver fibrosis. Interestingly, MafG knockdown increased HSCs ferroptosis, while MafG overexpression conferred resistance of HSCs to ferroptosis. Mechanistically, MafG physically interacted with non-muscle myosin heavy chain IIa (MYH9) to transcriptionally activate lipocalin 2 (LCN2) expression, a known suppressor for ferroptosis. Site-directed mutations of MARE motif blocked the binding of MafG to LCN2 promoter. Re-expression of LCN2 in MafG knockdown HSCs restored resistance to ferroptosis. In bile duct ligation (BDL)-induced mice model, we found that treatment with erastin alleviated murine liver fibrosis by inducing HSC ferroptosis. HSC-specific knowdown MafG based on adeno-associated virus 6 (AAV-6) improved erastin-induced HSC ferroptosis and alleviation of liver fibrosis. Taken together, MafG inhibited HSCs ferroptosis to promote liver fibrosis through transcriptionally activating LCN2 expression. These results suggest that MafG/MYH9-LCN2 signaling pathway could be a novel targets for the treatment of liver fibrosis.

INTRODUCTION

Liver fibrosis is an abnormal wound-healing response against various etiologies, including viral (HBV and HCV) related chronic liver disease, primary biliary cirrhosis (PBC), primary sclerosing cholangitis (PSC) and autoimmune liver disease (ALD) [1]. It is the major risk factor for liver failure and liver cancer [2]. Liver fibrosis is featured by the excessive production of ECM and destroy of physiological architecture [3]. The activated HSCs are the central driver underlying liver fibrogenesis and dominant source of ECM proteins secreting [4]. Since the activation of HSCs is influenced by diverse cytokines and signaling pathways, inhibition of HSCs activation is insufficient to reverse liver fibrosis [5]. Iron is abundant in activated HSCs [6]. Targeting the death of activated HSCs such as ferroptosis is a potential therapeutic way on the regression of liver fibrosis [7, 8].

Ferroptosis is a novel form of cell death caused by iron overload and lipid peroxidation, which is first described by Stockwell in tumor [9]. The morphological characteristics of ferroptosis comprise mitochondrial shrinking, increased electron density and mitochondrial membrane rupture [10]. Differing from classical programmed cell death in morphology, genetics and molecular mechanism, ferroptosis is unable to be suppressed by the inhibitors of apoptosis, necrosis and autophagy [11]. The homeostasis of iron pool is maintained by the transferrin, transferrin receptor, iron-storage protein ferritin and iron transporter [12]. When these proteins are abnormally expressed, labile iron pool leads to intracellular reactive oxygen species (ROS) accumulation via Fenton reaction, which directly catalyzes the formation of lipid peroxides and triggers ferroptosis [13]. Iron can also binds to glutathione (GSH), a scavenger of excessive ROS [14]. Ferroptosis is modulated at diverse levels including transcription factors [15]. Such transcription factors take part in prompt reactions to ferroptotic stimuli as well as regulation of ferroptosis long-term consequence in a context-dependent way [16]. For instance, nuclear protein 1 (NUPR1) blocks the oxidative damage of ferroptosis and is responsible for the anticancer resistance of ferroptosis inducer in pancreatic cancer [17]. The p53 serves a dual function in ferroptosis depending on the cancer type [18]. Although some advances have been achieved in understanding the role of transcription factors in ferroptosis, the pivotal transcription factor regulating ferroptosis in liver fibrosis remain unclear.

MafG is a basic leucine zipper transcription factor and belongs to small Maf proteins family that lack transactivation domain [19]. The homodimers within MafG function as transcriptional repressors while heterodimers with other proteins may act as

[1]Department of Ultrasonic Imaging, Xiangya Hospital, Central South University, Changsha 410008 Hunan, China. [2]Department of Oncology, NHC Key Laboratory of Cancer Proteomics & State Local Joint Engineering Laboratory for Anticancer Drugs, National Clinical Research Center for Geriatric Disorders, Xiangya Hospital, Central South University, Changsha 410008 Hunan, China. [3]Department of Thoracic Surgery, Xiangya Hospital, Central South University, Changsha 410008 Hunan, China. [4]Department of Infectious Disease, Xiangya Hospital, Central South University, Changsha 410008 Hunan, China. [5]Division of Digestive and Liver Diseases, Cedars-Sinai Medical Center, Los Angeles, CA, USA. [6]Department of Gastroenterology, Xiangya Hospital, Central South University, Changsha 410008 Hunan, China. ✉email: liuting818@csu.edu.cn; yonghenc@163.com

1128

transcriptional activators [20]. MafG heterodimerizes with members of the Cap 'n' Collar (CNC) transcription factor family (Nrf2 and BACH1) or interact with several different proteins, such as c-myc and c-Maf, to participate in multiple cellular processes [21, 22]. MafG can be induced by cholestatic liver injury [23], which is an important pre-pathological process of liver fibrosis. Oxidative damage is dramatically aroused during ferroptosis [24]. MafG is essential for activating antioxidant response and participates in regulating cellular ROS level [25, 26]. MafG has also been shown to be involved in ferroptosis in bladder cancer and hepatocellular carcinoma [27, 28]. However, the regulatory mechanism of MafG regulating ferroptosis in liver fibrosis has not been elucidated yet.

Here, we found that MafG interacts with MYH9 to transcriptionally regulate LCN2 in HSCs. Blockade of MafG decreases the transcription of LCN2, which causes iron accumulation and enhances the anti-fibrotic effect of ferroptosis inducer in vitro and in vivo.

METHODS AND MATERIALS
Animal models
8-12 week male C57BL/6 mice were purchased from the Central South University Animals Institute. Mice were raised under 12 h light and 12 h dark environment in cycle with 20-25℃ temperature and 40-60% humidity. Food and water are available for them at Central South University Animals center. Thirty mice were randomized into five groups with six animals in each. 100 μl AAV6-shControl or AAV6-shMafG (1×10^{12} viral genomes/mL) (Hanbio biotechnology, Shanghai, China) were injected into the mice through tail vain one week prior to liver fibrosis modeling. Liver fibrosis was induced by intraperitoneal injection of CCL_4 (Sigma-Aldrich, Missouri, USA, 1 μl/g body weight, diluted 1:3 in olive oil) twice per week for eight weeks or common bile duct ligation for 2 weeks. Control mice received equal volume of olive oil (Sigma-Aldrich, 1 μl/g body weight) or a sham operation in which abdominal cavity was exposed without ligation of common bile duct. For BDL animal model, mice were anesthetized and subjected to midline laparotomy. Common bile duct was separated and ligated near the liver hilus with 5-0 surgical silk, and then cut between the surgical ligatures. Imidazole ketone erastin (IKE) (40 mg/kg body weight) was administrated by intraperitoneal injection once every other day for two weeks following BDL operation. The mice were sacrificed and the livers were collected for subsequent analysis. All experimental procedures were carried out under the Central South University Animal Care and Use Committee criteria (#2022020206).

Human liver specimens and cell culture
24 liver biopsy samples were obtained from liver fibrotic/cirrhotic patients in Xiangya Hospital of Central South University, which included 10 individuals with hepatitis B virus (HBV) infection, 8 with PBC and 6 with PSC. The diagnosis of liver fibrosis referred to the guidelines of the American Association for the Study of Liver Diseases (AASLD). 10 normal liver samples were acquired from donors after liver transplantation. Informed consent from all the individuals was obtained and recorded. The research protocol conformed to the guidelines of ethical committees of the Xiangya Hospital of Central South University (#202004246). Basic information of patients in the study was available in supplementary table 1.

Human HSC LX-2 (CL-0560) and rat HSC-T6 (CL-0116) cell lines were bought from Procell Life science (Hubei, China). These cells were cultured in Dulbecco's Modified Eagle Medium (DMEM) (Gibco, Massachusetts, USA, 11965092) with 10% fetal bovine serum (FBS) (Gibco, 10100147C) and 1% antibiotics (Gibco, 15070063) and maintained at incubator of 37 ℃ with 5% CO_2 condition. The short tandem repeat profiling was used to identify cell lines.

Isolation of primary HSC, Kupffer cell and primary hepatocyte from murine liver
Murine primary HSCs, Kupffer cells and primary hepatocytes were separated as previously reported [29, 30]. Briefly, the murine livers were retrograde stepwise perfused and digested with DMEM-free solutions containing pronase (Sigma-Aldrich) and collagenase type I (Sigma-Aldrich). The cell suspension was collected and centrifuged to obtain supernatants. Primary HSCs, Kupffer cells and primary hepatocytes were isolated from supernatants through percoll density centrifugation and cultured in DMEM supplemented with 10% FBS.

Antibodies and reagents
Erastin (S7242), IKE (S8877), ferrostatin-1 (S7243), Z-VAD-FMK (S7023), ML385 (S8790), staurosporine (S1421) and rapamycin (S1039) were obtained from Selleck Chemicals(Texas, USA). The antibodies were detailed in supplementary table 2.

RNAi and transfection
Human MafG shRNA, pCMV-MafG plasmid (NM_002359.4), rat MafG shRNA and pCMV-MafG plasmid (NM_022386.3) were purchased from Genechem (Shanghai, China). The human LCN2 siRNA, pCMV-LCN2 plasmid (NM_005564.5), MYH9 siRNA, p50 siRNA and p65 siRNA were purchased from RIBBIO (Guangdong, China). Transfections of plasmid, shRNA and siRNA were performed with jetPRIME (Polyplus, Strasbourg, France, 101000027) according to the manufacturer's instructions. The sequence of shRNA and siRNA were listed in supplementary table 3.

Real-time polymerase chain reaction (PCR)
Total RNA was extracted from cells or liver tissues by Trizol reagent (Invitrogen, Canifornia, USA) and reverse transcribed into cDNA using HiScript III RT SuperMix (Vazyme, Jiangsu, China). Quantitative real-time PCR was conducted using ChamQ Universal SYBR qPCR Master Mix (Vazyme). The $2^{-\triangle\triangle CT}$ method was applied to calculate the value of gene expression level. The relative quantifications of mRNA were expressed in random parts based on the control group that was designated to the value of 1. The sequences of specific primers were available in Supplementary Table 4.

Western blot analysis
The protein of liver tissues and cells were extracted using 1× RIPA buffer (Sigma-Aldrich) with protease inhibitor cocktail (Sigma-Aldrich). Protein quantification was determined by BCA protein assay kit (Sigma-Aldrich). The 20-40 μg protein of each sample was loaded on SDS-PAGE (Bio-Rad, Canifornia, USA) and separated in running buffer. Then protein was transferred to polyvinylidene fluoride (PVDF) membranes (Bio-Rad) and subsequently blocked in 5% non-fat milk for 1 h. The PVDF membranes were incubated with diverse primary antibodies at 4℃ overnight and corresponding peroxidase conjugated secondary antibodies at room temperature for 1 h. The bands were visualized through the chemiluminescence (Syngene G:BOX, USA). Image J application was used to analyze the intensities of protein bands.

Histological analysis
The human and animal liver tissues were fixed in formalin for 24 h and embedded in paraffin. The paraffin blocks were cut to a thickness of 5 μm for subsequent histopathological examination. Five micrometers sections were performed with hematoxylin & eosin (H&E) and Picro Sirius Red (PSR) staining. For immunohistochemistry (IHC), paraffin sections were incubated with various primary antibodies at 4℃ overnight and colored by 3,3'-diaminobenzidine chromogen. The intensity and ratio of PSR and IHC staining were evaluated by two independent pathologists.

Luciferase reporter assay
The mutation of MafG binding site in LCN2 promoter was conducted as follows: 5'-TCAGCA-3' (-655 to -660) was altered to 5'-TCAATA-3'. The human LCN2 promoter and LCN2 promoter mutant were cloned into pGL3-Basic vector respectively. The MafG plasmid or MafG siRNA and promoter constructs were co-transfected into LX-2 cells with jetPRIME reagent. 24 h after transfection, Dual-Luciferase Reporter Assay System (Promega, Wisconsin, USA) was used to measure the luciferase activity on a Perkin Elmer luminometer according to the manufacturer's protocol. The transcriptional activity was quantified by the ratio of firefly luciferase intensity to Renilla luciferase intensity.

Chromatin immunoprecipitation (ChIP) assay
ChIP was carried out according to the manufacturer's instruction of ChIP assay kit (Thermo Fisher Scientific, Canifornia, USA, 26159). Briefly, the DNA was cross-linked by 37% formaldehyde and digested into chromatin fragments by nuclease. The DNA was immunoprecipitated with MafG or

IgG antibody. The chromatin fragments were purified and finally analyzed by real-time PCR assay. Real-time PCR primers of the LCN2 promoter region containing MafG binding site were as follows: forward 5′-TGTCCAGAG-CAGCAGTGTG -3′, reverse 5′- CTCTCCTGTGAGTGCAGTGG -3′.

Electrophoretic mobility shift assay (EMSA)

The DNA probe for EMSA were double-strand MafG element (5′-CTGTAGCCTCAGCA-3′, −655/−668) and mutative MafG element (5′-CTGTAGCCTCAATA -3′, −655/−668) in the LCN2 promoter relative to the TSS. Binding reactions were conducted in the EMSA buffer (20 mM HEPES, 200 mM NaCl, 10 mM $MgCl_2$, 1 mM EDTA, 0.1 mM DTT, and 0.5% TritonX-100). 1.2 µM DNA probe was loaded onto the 8% native polyacrylamide gel with varied concentrations of MafG recombinant protein according to the molar ratio of protein to DNA. The signals of bands were visualized with a ChemiDoc XRS scanner (Bio-Rad).

Cell viability

Cell viability assay was performed by CCK8 Cell Counting kit (Vazyme). Briefly, LX-2 and HSC-T6 cells were seeded into 96-well plates and treated with indicated compounds. 100 µl fresh medium containing 10 µl CCK8 reagents were added to each well. Next cells were incubated at 37℃ with 5% CO_2 for 2 h. Microplate reader (BioTek, Vermont, USA) was used to detect the absorbance of 450 nm.

Biochemical assay

The concentrations or activity of MDA (Abcam, Cambridge, UK, ab118970), iron (Abcam, ab83366), GSH (Bestbio, Shanghai, China, BB-4711), AST (Abcam, ab263882) and ALT (Abcam, ab282882) were measured by commercially available kit following manufacturer's protocol. Microplate reader (BioTek) was applied to detect the absorbance of samples. For lipid ROS, follow the kit protocol (Thermo Fisher Scientific, D3861) and upon completion observe the cells immediately using emission filter appropriate for fluorescence. Image J was applied to analyze the intensity of fluorescence.

Mass spectrometry (MS) and co-immunoprecipitation (co-IP)

LX-2 cells were treated with erastin (10 µM) for 24 hours and lysed in 1% TritonX-100 (Sigma-Aldrich) buffer supplemented with protease inhibitor cocktail (Roche, Basel, Switzerland). Total protein was immunoprecipitated with MafG or IgG antibody and A/G plus agarose beads (Santa Cruz Biotechnology, Canifornia, USA) overnight at 4℃. The beads coupled complexes were washed with TritonX-100 buffer for 3 times and used for MS identification. For co-IP, the complexes were boiled for denaturation and subjected to SDS-PAGE.

Extraction of nuclear protein

The cytosolic and nuclear proteins from the LX-2 cells were prepared by NE-PER nuclear and cytoplasmic extraction reagents (Thermo Fisher Scientific, 78835) based on the manufacturer's instruction. Succinctly, LX-2 cells wered harvested with trypsin-EDTA and then centrifuge for 5 min. The ice-cold CER II was added to the tube, mixed thoroughly, incubated on ice and centrifuged. The remaining insoluble fraction that contains nuclei was suspended in the ice-cold NER. The sample was then vortexed and centrifuged at maximum speed. The supernatant was collected for following co-IP experiment.

Immunofluorescence assay

The 4% formalin fixed LX-2 cells or paraffin sections were permeabilized with 0.1% TritonX-100 at room temperature for 20 minutes. Samples were blocked in 5% bovine serum albumin (BSA) (Sigma-Aldrich) for 60 min and then incubated with primary antibody overnight. Fluorescent secondary antibodies (Abcam) were added to the dishes and incubated for 1 h at room temperature. Nuclei were stained by DAPI (Abcam). The cells were photographed under fluorescence confocal microscope (Carl Zeiss, Jena, Germany).

Statistical analysis

The data from three independent experiments were shown as mean ± standard error of mean (SEM). Software Prism 8.2.1 was applied to analyze data. All tests performed were two-sided. The comparisons between two groups were analyzed by unpaired Student's t-test. A one-way analysis of variance (ANOVA) with Student-Newman-Keuls test was employed for comparisons among multiple groups. The p value of <0.05 was rendered as statistical significance.

RESULTS

MafG expression level is upregulated in liver fibrosis

To determine the MafG protein level in liver fibrosis, MafG expression was compared in the human liver fibrotic/cirrhotic samples with those of healthy donors. Hepatic fibrosis was verified by H&E staining and PSR staining in human liver tissues (Fig. 1A). The protein level of MafG was obviously upregulated in fibrotic/cirrhotic liver specimens from patients with HBV infection, primary biliary cirrhosis (PBC) and primary sclerosing cholangitis (PSC) (Fig. 1A, B). Furthermore, two well-established liver fibrosis murine models were built up through CCL_4 injection and bile duct ligation (BDL) [31]. The murine fibrotic liver tissues demonstrated stronger MafG staining (Fig. 1C) and much more MafG expression (Fig. 1D) than liver samples in control group. In fibrotic tissues, we noticed that the MafG staining was positive around bile ducts that were surrounded by myofibroblasts [32]. This suggested that MafG might be upregulated in myofibroblasts activated in fibrosis. To confirm MafG expression in activated HSCs which are the main cell type of myofibroblasts, we co-stained MafG with α-SMA, the cell marker of activated HSCs, in patient fibrotic liver tissues. We found that MafG expression was co-localized with α-SMA, implying that MafG was increased in activated HSCs (Supplementary Fig. 1A). Similar findings were observed in murine fibrotic liver tissues(Supplementary Fig. 1B). Next, we knockdown MafG expression level in human hepatic stellate cell line LX-2 and rat hepatic stellate cell line HSC-T6. Downregulated MafG substantially gave rise to reduced mRNA and protein levels of α-SMA and COL1A1, which were classic fibrotic markers (Fig. 1E, Supplementary Fig. 2A). Conversely, enhancement of MafG expression was consistent with significant increase of α-SMA and COL1A1 in both mRNA and protein levels (Fig. 1F, Supplementary Fig. 2B). In conclusion, these results implied that MafG expression was induced during the development of liver fibrosis. The expression of MafG was enhanced by nuclear factor-kappa B (NF-κB) through binding to the NF-κB sites located on MafG promoter in cholestatic liver injury [23]. Notably, the knockdown of NF-κB (p50/p65), key transcription factors involved in driving liver fibrosis [33], decreased protein and mRNA levels of MafG and COL1A1 in LX-2 cells (Supplementary Fig. 3A, B). These findings indicated that NF-κB facilitated the upregulation of MafG in liver fibrosis.

MafG is a repressor of ferroptosis in liver fibrosis

MafG plays an important role in modulating ROS that is crucial for the process of cell death, including ferroptosis, apoptosis and autophagy [25, 34]. To explore the role of MafG in these types of cell death, we first determined MafG expression levels during HSC ferroptosis, apoptosis and autophagy. The preclinical drug erastin, staurosporine and rapamycin can trigger ferroptosis, apoptosis and autophagy in HSCs [7, 35, 36]. Notably, the erastin treatment significantly decreased protein level of MafG, α-SMA, COL1A1 and GPX4, a well-known ferroptosis marker, in a dose-dependent manner while staurosporine and rapamycin exerted no effect on MafG expression (Fig. 2A, Supplementary fig. 4A), suggesting that MafG might participate the ferroptosis of HSCs. Moreover, MafG knockdown dramatically enhanced the sensitivity of LX-2 and HSC-T6 to ferroptotic death induction by erastin, which were indicated by attenuated protein levels of α-SMA and COL1A1 (Fig. 2B). The morphological characteristics of ferroptotic cells are mitochondrial shrinkage, increased electron density and loss of mitochondrial ridge [37]. In accordance with previous results, MafG knockdown obviously increased the degree of morphological changes in ferroptotic HSC mediated by erastin (Fig. 2C). In addition, decreased MafG expression greatly contributed to
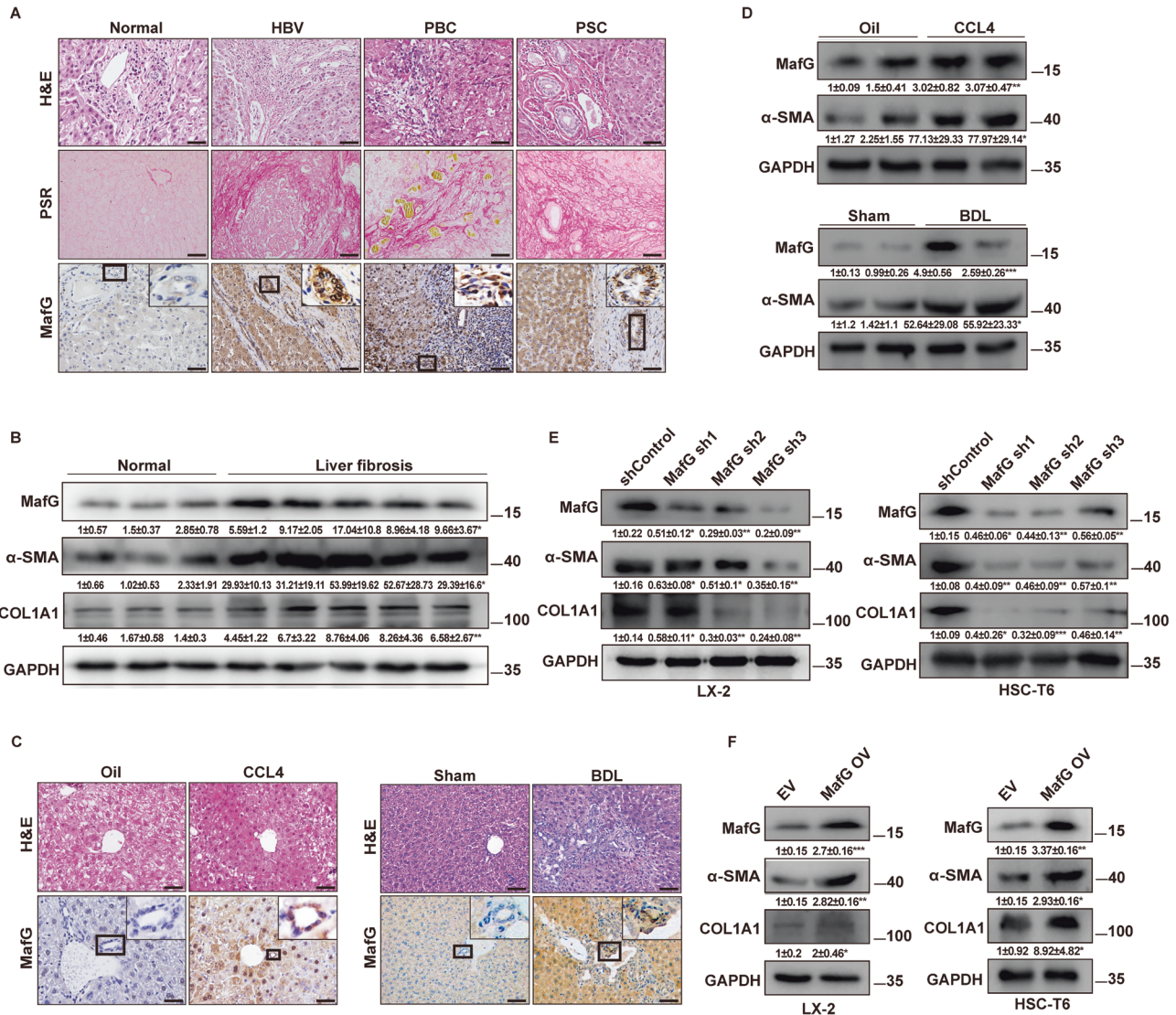
Fig. 1 The expression level of MafG is upregulated in liver fibrosis. A Representative images of IHC for MafG, H&E and PSR staining in liver tissues from human healthy donors and patients diagnosed with HBV-related liver fibrosis, PBC and PSC. Scale bar, 50 μm. **B** Western blot for MafG, α-SMA and COL1A1 in human normal liver tissues and fibrotic liver tissues. GAPDH was loaded as an internal reference for western blot (also in other western blot assays). Numbers below the Western blots are densitometric values expressed as ratio of normal liver. **C** Representative images of IHC for MafG and H&E staining in murine oil control group and CCL₄ model group, murine sham group and BDL model group. Scale bar, 50 μm. **D** Western blot for MafG and α-SMA in murine liver tissues from control group and CCL₄- and BDL- models. Numbers below the blots are densitometric values expressed as the ratio of control group. **E** Western blot for MafG, α-SMA and COL1A1 in control and shRNA based MafG knockdown (MafG sh) LX-2 and HSC-T6 cells. shControl indicated a non-target scramble shRNA and was applied as a negative control. Numbers below the blots are densitometric values expressed as ratio of shControl. **F** Western blot for MafG, α-SMA and COL1A1 in LX-2 and HSC-T6 transfected with empty vector or MafG plasmid. Numbers below the blots are densitometric values expressed as ratio of EV. The results were represented by mean ± SEM with corresponded significance. *$P < 0.05$, **$P < 0.01$, ***$P < 0.001$, ns not significant. The results were repeated in three independent experiments.

erastin-induced iron accumulation (Fig. 2D), lipid peroxidation (Fig. 2E), growth inhibition (Supplementary Fig. 4B, C), GSH exhaustion (Supplementary Fig. 4D), and lipid ROS production (Fig. 2F). In contrast, MafG plasmid mediated MafG overexpression abolished these classic ferroptotic events and conferred resistance to erastin-mediated reduction of fibrotic markers in HSCs (Fig. 3A-F). Furthermore, the ferrostatin-1 (a ferroptosis inhibitor) remarkably reversed erastin-induced ferroptotic events in LX-2 and HSC-T6. However, the Z-VAD-FMK (a apoptosis inhibitor) were not able to reverse the process of ferroptosis (Figs. 2B, D-E, 3A-E, Supplementary fig. 4B-D). Taken together, these findings provided evidences that MafG regulated ferroptosis in HSC rather than apoptosis.

LCN2 is an effector gene of MafG in regulating ferroptosis
As a transcription factor, MafG binding site has previously been identified (Fig. 4A) [38]. To further explore the potential mechanism of MafG in regulating ferroptosis, MafG ChIP-seq database GSE92076 have been used to confirm the target gene of MafG in modulating ferroptosis. Seven of the twenty-eight candidates that have been widely proved to participate in ferroptosis [10, 39], including LCN2, FTL, FTH1, TFRC, FPN, STEAP3 and ELOVL6, were identified in dataset GSE92076 (Fig. 4B, Supplementary table 5). Among those genes, MafG knockdown obviously suppressed the LCN2 mRNA level in LX-2 (Fig. 4C, D). We therefore focused on LCN2. LCN2, an iron transporter, is essential for modulating labile iron pool, which is a potent redox engine and can lead to lipid ROS
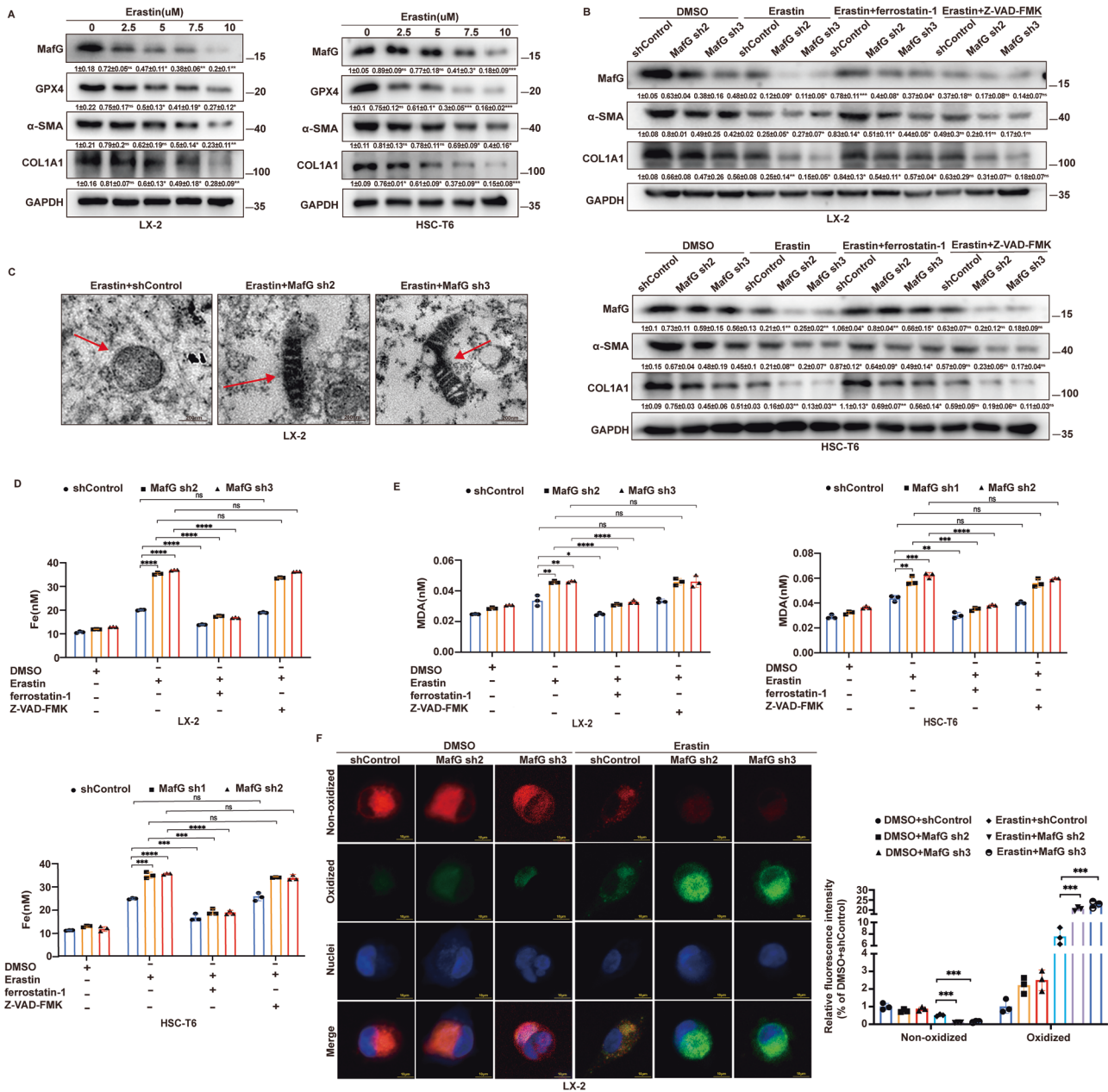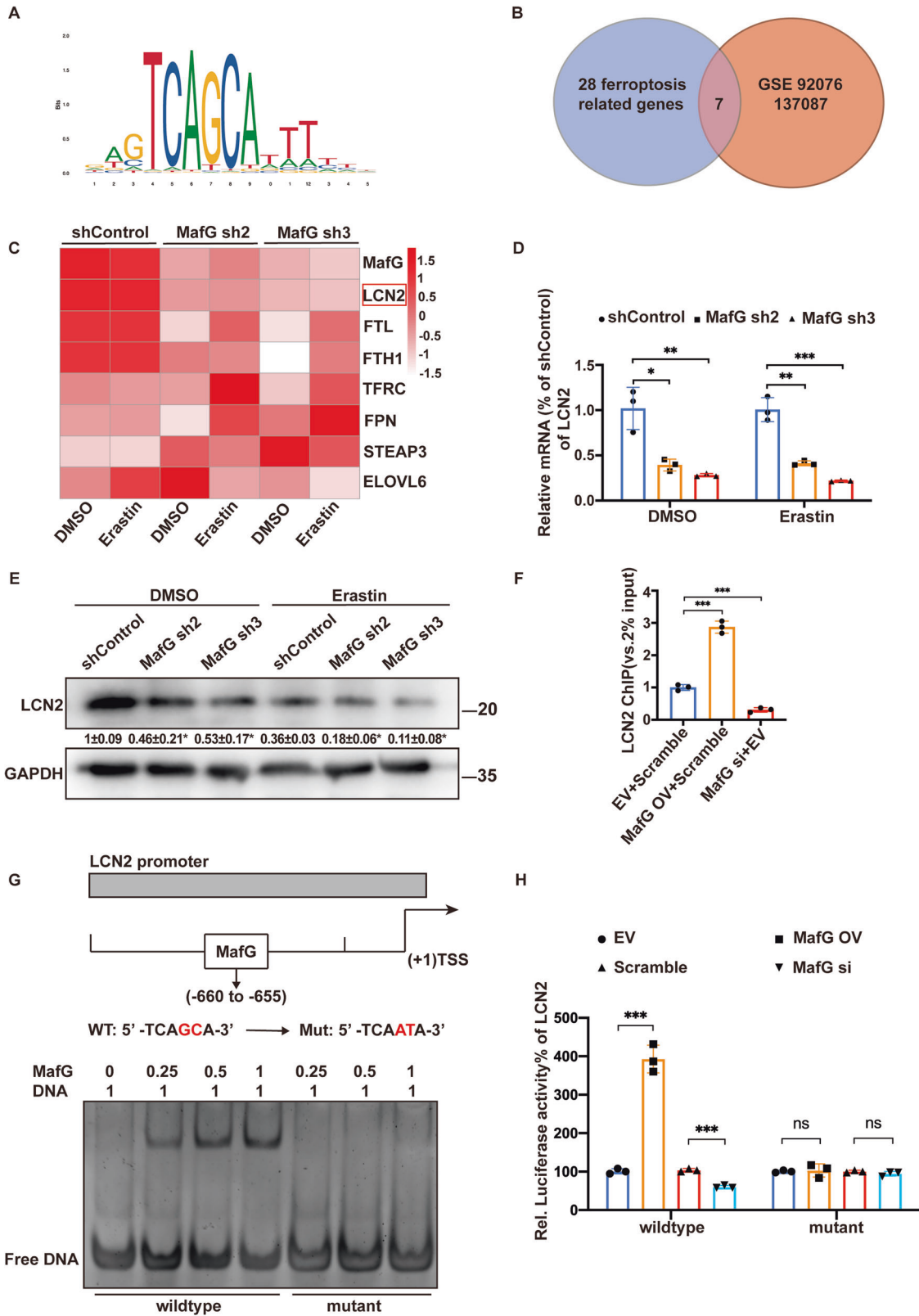
Fig. 2 MafG knockdown promotes erastin-mediated HSC ferroptosis. A Western blot for MafG, GPX4, α-SMA and COL1A1 in wildtype LX-2 and HSC-T6. Cells were exposed to different concentration of erastin (0, 2.5, 5, 7.5, 10 μM) for 24 h. Numbers below the blots are densitometric values expressed as ratio of 0 μM. **B** LX-2 and HSC-T6 cells were exposed to vehicle (0.01% dimethyl sulfoxide) or erastin (10 μM) with or without indicated inhibitors (ferrostatin-1, 5 μM; Z-VAD-FMK,10 μM) for 24 h following transfection with shControl or MafG targeting shRNA. Protein levels of MafG, α-SMA and COL1A1 were detected by western blot. Numbers below the blots are densitometric values expressed as ratio of DMSO+shControl. **C** Representative images of control and MafG knockdown LX-2 cells treated with erastin (10 μM) for 24 h observed under transmission electron microscope. Scale bar, 200 nm. **D–E** The levels of intracellular iron (**D**) and MDA (**E**) of LX-2 and HSC-T6 cells were examined. Cells were treated in the same way as (**B**). **F** Representative fluorescence images of lipid ROS (left panel) in LX-2 cells of indicated groups. Scale bar, 10 μm. The relative fluorescence intensity was measured (right panel). Cells were treated with vehicle (0.01% dimethyl sulfoxide) or erastin (10 μM) for 24 h. Data were represented by the mean ± SEM with corresponded significance. *$P < 0.05$, **$P < 0.01$, ***$P < 0.001$, ns not significant. The results were repeated in three independent experiments with three replicate each.

generation [40]. Consistent with the mRNA assay, downregulated protein level of LCN2 resulted from reduced MafG expression level was verified in erastin-treated HSC group and control group (Fig. 4E). As expected, NF-κB (p50/p65) knockdown suppressed LCN2 protein and mRNA levels in LX-2 cells, which might indicated that NF-κB-dependent MafG expression is necessary for downstream LCN2 expression in HSCs (Supplementary Fig. 3A, B). MafG binding site was found to be contained in the promoter sequence

of LCN2 (Supplementary Fig. 5A). Next, a chromatin immunoprecipitation (ChIP) assay was performed to determine whether MafG functioned by binding directly to the LCN2 promoter. Enhancement of MafG remarkably increased its binding while silencing MafG caused loss of binding (Fig. 4F). Moreover, MafG was unable to bind directly to LCN2 promoter mutants of MafG binding site on EMSA (Fig. 4G). Wildtype LCN2 promoter activity was also significantly reinforced by MafG overexpression by three-fold and
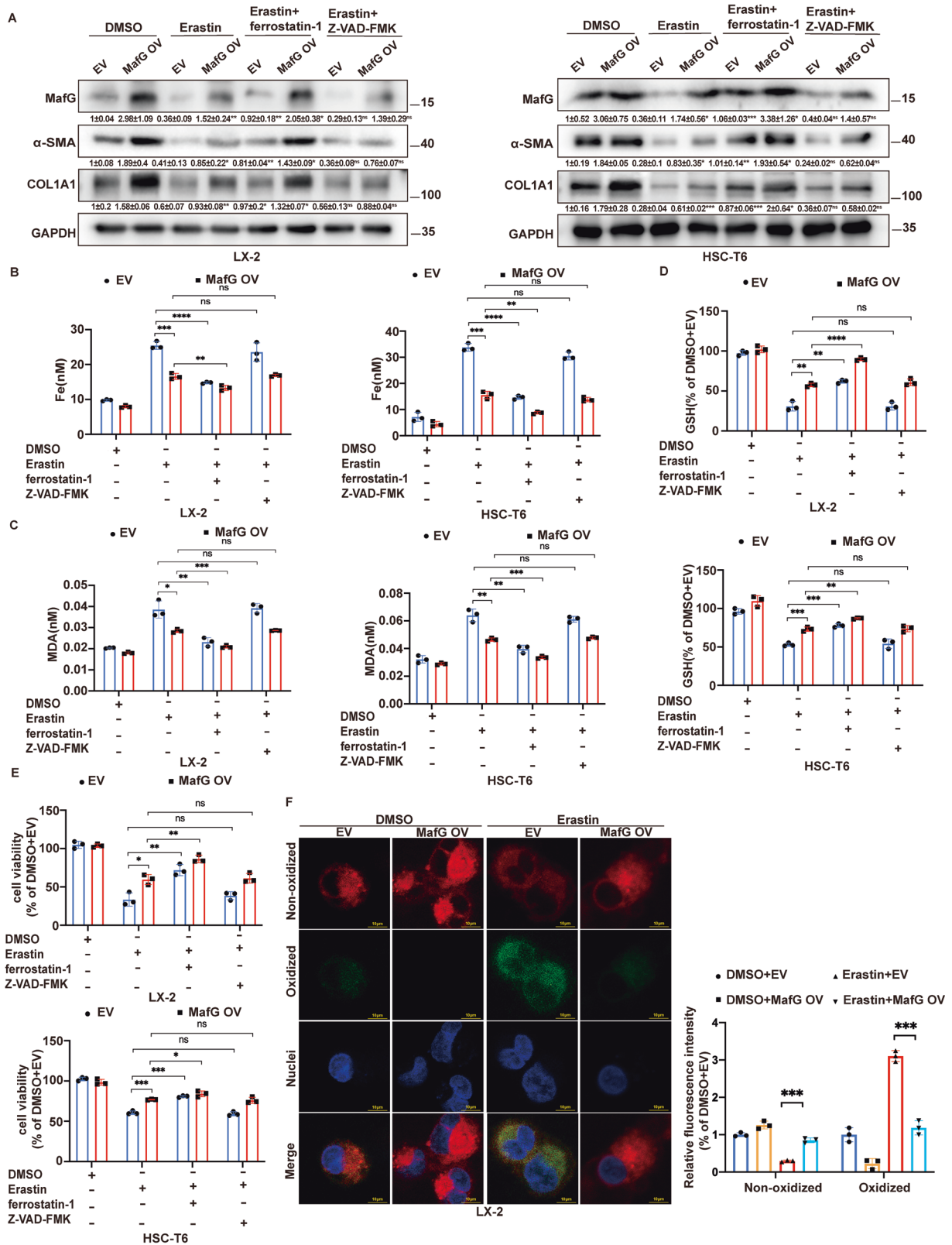
Fig. 3   MafG overexpression inhibits erastin-induced ferroptosis in HSC. A-E LX-2 and HSC-T6 cells were exposed to vehicle (0.01% dimethyl sulfoxide) or erastin (10 μM) with or without indicated inhibitors (ferrostatin-1, 5 μM; Z-VAD-FMK,10 μM) for 24 h following transfection with empty vector (EV) or MafG plasmid (MafG OV). Protein levels of MafG, α-SMA and COL1A1 were assayed by western blot (**A**). Numbers below the blots are densitometric values expressed as ratio of DMSO + EV. The levels of intracellular iron (**B**), MDA (**C**), GSH (**D**) and cell viability (**E**) were quantifed. **F** Representative fluorescence images of lipid ROS (left panel) in LX-2 of indicated groups. Scale bar, 10μm. The relative fluorescence intensity was measured (right panel). Cells were treated with vehicle (0.01% dimethyl sulfoxide) or erastin (10 μM) for 24 h. Data were represented by the mean ± SEM with corresponded significance. *$P < 0.05$, **$P < 0.01$, ***$P < 0.001$, ns: not significant. The results were repeated in three independent experiments with three replicate each.

A

B

C shControl | MafG sh2 | MafG sh3

MafG 1.5 1 0.5 0 -0.5 -1 -1.5
LCN2
FTL
FTH1
TFRC
FPN
STEAP3
ELOVL6

DMSO | Erastin | DMSO | Erastin | DMSO | Erastin

D
• shControl ■ MafG sh2 ▲ MafG sh3

Relative mRNA (% of shControl) of LCN2

E
DMSO | Erastin

LCN2 —20
1±0.09 0.46±0.21* 0.53±0.17* 0.36±0.03 0.18±0.06* 0.11±0.08*
GAPDH —35

F
LCN2 ChIP(vs.2% input)

G
LCN2 promoter

MafG

(-660 to -655)   (+1)TSS

WT: 5′-TCAGCA-3′ ⟶ Mut: 5′-TCAATA-3′

MafG 0 0.25 0.5 1 0.25 0.5 1
DNA   1 1   1   1 1   1   1

Free DNA

wildtype | mutant

H
• EV ■ MafG OV
▲ Scramble ▼ MafG si

Rel. Luciferase activity% of LCN2

wildtype | mutant

repressed by knockdown of MafG (Fig. 4H). Importantly, alteration of MafG expression level no longer exerted any effect on the LCN2 promoter when MafG binding site was mutated. These findings suggested that MafG regulated LCN2 expression at transcriptional level in HSCs during ferroptosis.

Silencing MafG promotes ferroptosis of HSC through LCN2
We next determined whether the LCN2 has a similar phenotype in liver fibrosis and ferroptosis to that of MafG. Indeed, LCN2 expression was upregulated in human liver fibrotic samples (Fig. 5A) and murine fibrotic liver tissues (Supplementary Fig. 5B).

Fig. 4 LCN2 is an effector gene of MafG in regulating ferroptosis. A DNA matrix of MafG binding sites obtained from JASPAR (https://jaspar.genereg.net/). **B** The number of potential MafG target genes in ferroptosis identified in MafG ChIP-seq data. **C** Heatmap of relative mRNA levels of ferroptosis-related genes in control and MafG knockdown LX-2 cells following exposure to vehicle (0.01% dimethyl sulfoxide) or erastin (10 μM) for 24 h. **D–E** Real-time PCR (**D**) and western blot (**E**) for LCN2 in control and MafG knockdown LX-2 cells following exposure to vehicle (0.01% dimethyl sulfoxide) or erastin (10 μM) for 24 h. Numbers below the blots are densitometric values expressed as ratio of DMSO +shControl. **F** ChIP analysis detecting binding of MafG to the LCN2 promoter in control, MafG overexpression and MafG knockdown LX-2 cells. **G** EMSA analysis monitoring binding of MafG to the LCN2 promoter wildtype and LCN2 promoter mutant. The mutation sites on LCN2 promoter were shown in red font. **H** Luciferase reporter analysis for control, MafG overexpression and MafG knockdown LX-2 cells after transfection with pGL3-luciferase construct. Renilla values were used as reference. Values were normalized to empty vector control group or scramble control group. Data were represented by the mean ± SEM with corresponded significance. $*P < 0.05$, $**P < 0.01$, $***P < 0.001$, ns not significant. The results were repeated in three independent experiments with three replicate each.

Moreover, LCN2 overexpression increased the protein levels of component of extracellular matrix (COL1A1) and marker of activated hepatic stellate cells (α-SMA) in LX-2. In contrast, LCN2 silence greatly attenuated the protein expression levels of α-SMA and COL1A1 (Supplementary fig. 5C). Furthermore, enforced expression of LCN2 decreased erastin-induced extracellular matrix reduction (Fig. 5B), iron accumulation (Fig. 5C), lipid peroxidation (Fig. 5D), GSH depletion (Fig. 5E), cell death (Fig. 5F) and ROS generation (Fig. 5G). Hence, LCN2 acts the similar way as MafG in the liver fibrosis during ferroptosis.

To examine whether the reduced level of LCN2 is critical for MafG suppression in the induction of ferroptosis, we re-expressed LCN2 in siRNA-based MafG knockdown LX-2 by transfecting LCN2 plasmid. Compared with erastin-treated MafG silence group, the enhancement of LCN2 restored ferroptosis repression in LX-2 cells, which was linked with attenuated extracellular matrix reduction (Fig. 5B), iron accumulation (Fig. 5C), lipid peroxidation (Fig. 5D), GSH depletion (Fig. 5E), growth inhibition (Fig. 5F) and ROS production (Fig. 5G). Therefore, MafG silence promote ferroptosis in HSC via downregulating the expression of iron transporter LCN2.

MYH9 is required for MafG in transcriptional regulation of LCN2

MafG usually needs to be coupled with another partner to exert transcriptional activation activity [20]. To confirm the cooperator involved in MafG-directed targeting of LCN2 during ferroptosis, mass spectrometry was performed to determine the MafG interacting proteins in LX-2 cells. Top twenty proteins were identified in mass spectrometry analysis (Fig. 6A). The expression level of eight of these proteins (MYH9, ACTN4, ANXA2, CFL1, FLNA, HARS1, PKM and VIM) were found to be positively correlated with LCN2 expression level by further analyzing human hepatic fibrosis dataset GSE14323 (Fig. 6B). Among eight proteins that interacting with MafG, MYH9 was previously evidenced to be localized in nuclei and modulate gene transcription [41], which indicated that MYH9 might be indispensable for MafG to regulate LCN2 expression at transcriptional level (Fig. 6C). Moreover, silencing MYH9 substantially inhibited the LCN2 expression on protein level (Fig. 6D) and mRNA level (Fig. 6E) in HSCs. Co-immunoprecipitation assay showed that MafG antibody and MYH9 antibody pulled down each other in LX-2 from whole cell lysates (Fig. 6F) and nuclear extracts (Supplementary Fig. 6A). Immunofluorescence assay further confirmed the co-localization of MafG and MYH9 in the HSC nucleus (Fig. 6G). The interaction between MafG and MYH9 was modeled by molecular docking, in which the formation of hydrophobic bond and hydrogen bonds between amino acid of MafG and MYH9 were predicted (Supplementary Fig. 6B). Consistent with MafG silence, MYH9 knockdown remarkably reduced the binding of MafG on LCN2 promoter by ChIP (Fig. 6H). Additionally, Nrf2, a CNC family transcription factor, was well recognized as the heterodimerizing partner in MafG mediated transcription [19]. However, ML385 (a specific Nrf2 inhibitor) was unable to affect LCN2 expression while MafG overexpression significantly augmented the expression level

of LCN2 in HSCs (Supplementary fig. 6C). In summary, MafG cooperates with MYH9 to target LCN2 during ferroptosis, which are independent of Nrf2.

MafG limits the IKE-induced HSC ferroptosis in murine hepatic fibrosis

To evaluate whether the inhibition of MafG can augment the in vivo ferroptosis induced by IKE, a metabolically stable analog of erastin [42], we established a classical murine hepatic fibrosis model by BDL [43]. It was documented that AAV6 demonstrated organ tropism for activated HSCs in the progression of liver fibrosis [44]. Therefore, the AAV6 carrying shRNA targeting MafG (AAV6-shMafG) and AAV6 carrying non-targeting control vector expressing GFP (AAV6-shControl) were administrated to the murine fibrosis models. The histopathologic examination including H&E staining and PSR staining indicated that the fibrotic liver injury and collagen deposition were alleviated upon IKE treatment (Fig. 7A). The improving effect of IKE on histological analysis of hepatic fibrosis was obviously enhanced by AAV6-shMafG treatment in comparison with AAV6-shControl group (Fig. 7A). Furthermore, MafG knockdown in vivo conferred ferroptosis sensitivity of IKE that was associated with increased MDA level (Fig. 7B) or iron accumulation (Fig. 7C), decreased serum level of hepatic fibrosis markers (ALT and AST) (Fig. 7D) as well as reduced mRNA or protein levels of extracellular matrix (COL1A1) and marker of activated hepatic stellate cells (α-SMA) (Fig. 7E, F). Moreover, in accordance with in vitro observation, administration of AAV6-shMafG significantly decreased protein and mRNA levels of LCN2 in the liver of murine fibrosis model (Fig. 7E, F).

Recent study has implied that ferroptosis inducer erastin triggered ferroptosis process in HSCs rather than hepatocytes and macrophages during liver fibrosis [37]. We also found that MafG knockdown by siRNA facilitated erastin-mediated the decline of COL1A1 and α-SMA in primary HSCs separated from BDL-induced liver fibrosis murine model (Supplementary Fig. 7A). To further explore the function of MafG in IKE-induced HSC ferroptosis, we next isolated primary HSCs, Kupffer cells and primary hepatocytes from murine livers in sham, BDL + AAV6-shControl, BDL + AAV6-shMafG, BDL + AAV6-shControl+IKE and BDL + AAV6-shMafG+IKE group respectively. The AAV6-shMafG distinctly inhibited MafG protein and mRNA levels in primary HSCs instead of Kupffer cells and primary hepatocytes. HSC-specific inhibition of MafG remarkably promoted IKE-triggered reduction of COL1A1, α-SMA and LCN2 expression levels. In BDL group, IKE treatment was unable to alter MafG expression in Kupffer cells and primary hepatocytes (Fig. 7G, H, Supplementary Fig. 7B, C). Collectively, these results indicated that targeting MafG with AAV6 in HSCs contributed to IKE-induced HSC ferroptosis in murine hepatic fibrosis.

DISCUSSION

The transcription factors are indispensable for human physiology and disease, emphasizing the significance of comprehending gene expression regulation in multiple biological processes,
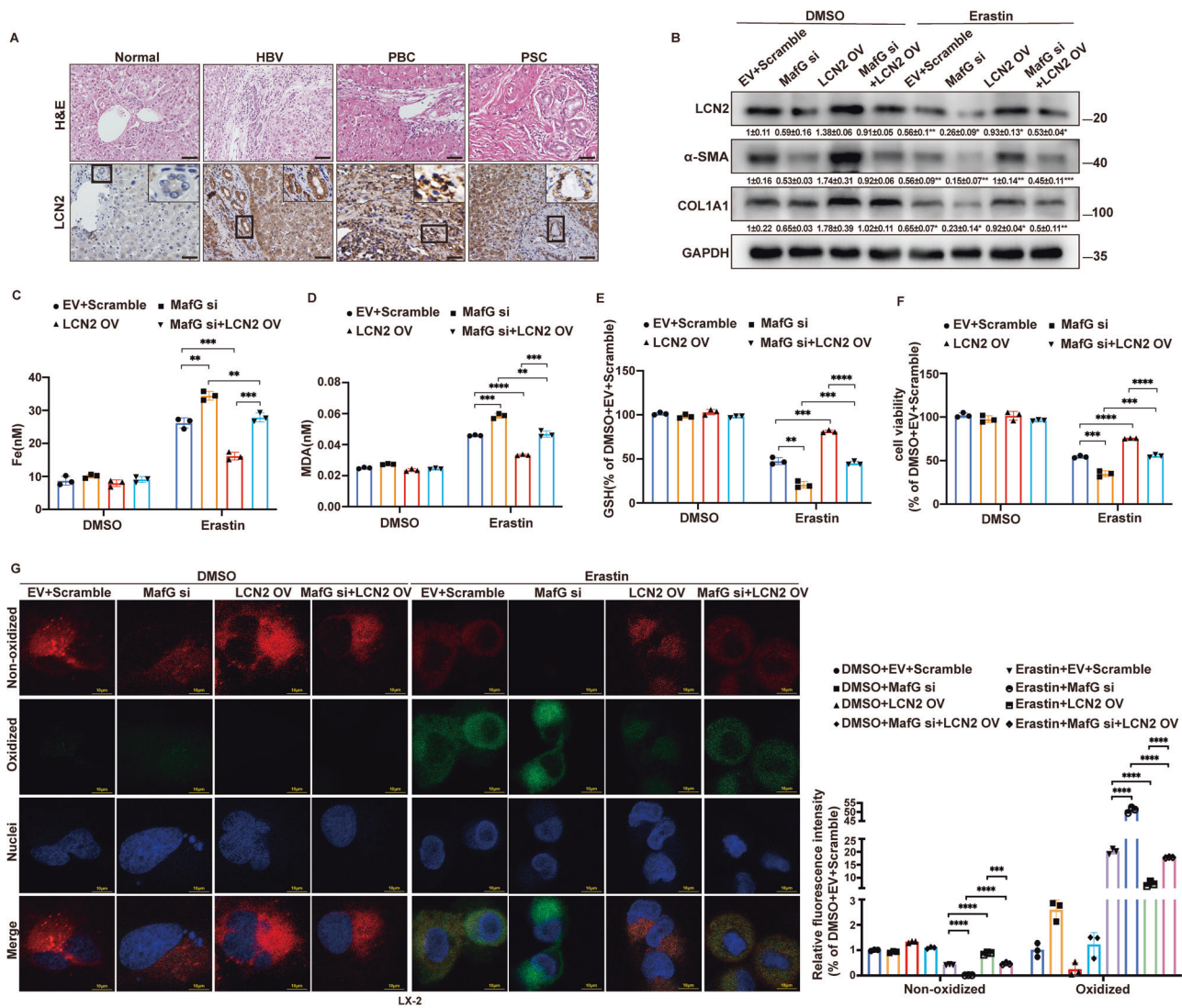
Fig. 5 Silencing MafG contributes to ferroptosis of HSC through LCN2. A Representative images of IHC for LCN2 and H&E staining in liver tissues from human healthy donors and patients diagnosed with HBV-related liver fibrosis, PBC and PSC. Scale bar, 50 μm. **B** Western blot for LCN2, α-SMA and COL1A1 in indicated LX-2 cells after exposure to vehicle (0.01% dimethyl sulfoxide) or erastin (10 μM) for 24 h. Numbers below the blots are densitometric values expressed as ratio of DMSO + EV+Scramble. **C–F** The levels of intracellular iron (**C**), MDA (**D**), GSH (**E**) and cell viability (**F**) were examined in indicated LX-2 cells after treated with vehicle (0.01% dimethyl sulfoxide) or erastin (10 μM) for 24 h. **G** Representative fluorescence images of lipid ROS (left panel) in LX-2 of indicated groups. Scale bar, 10 μm. The relative fluorescence intensity was measured (right panel). Cells were treated in the same way as (**B–F**). Data were represented by the mean ± SEM with corresponded significance. *$P < 0.05$, **$P < 0.01$, ***$P < 0.001$, ns: not significant. The results were repeated in three independent experiments with three replicate each.

including cell death [45]. In this research, we showed that blockade of MafG plays a key role in regulating a transcriptional program that enhances ferroptosis via downregulating LCN2 expression, indicating a potential approach for targeting ferroptosis in the treatment of disease.

Ferroptosis involves excessive production of iron-mediated accumulation of lipid ROS, the process of which are able to be pharmacologically repressed by inhibitors of lipid peroxidation and iron chelators [46]. Increasing evidences have proved the strategy for ferroptosis in preventing and regressing liver fibrosis [47]. For example, natural drugs including artesunate and magnesium isoglycyrrhizinate inhibited HSCs activation and alleviated liver fibrosis through ferroptosis signaling pathway [47, 48]. Moreover, RNA-binding protein ELAVL1 augmented HSC ferroptosis by activating autophagosome generation and autophagic flux [7]. Furthermore, BRD7 enhanced p53 mitochondrial translocation and interaction between p53 and solute carrier

family 25 member 28 (SLC25A28), which contributed to iron overload-induced oxidative damage and ferroptosis in HSCs [37]. Consistently, our study found that the triggering HSCs ferroptosis ameliorated the liver fibrotic manifestation. However, some challenges still remain in developing ferroptosis into a proven treatment for liver fibrosis. The ferric citrate, a ferroptosis stimuli, strongly induced ferroptosis of murine primary hepatocytes and macrophages, which might aggravate the liver injury [49]. Hence, development of drugs that specifically trigger ferroptosis in HSCs is needed in the future.

The upregulation of MafG has been previously verified in cholestasis mediated liver injury, a pre-stage of liver fibrosis, and liver cancer, the end stage of hepatic fibrosis [23, 50], which suggests that MafG is critical for the progression of liver fibrosis. Indeed, we discovered that MafG was highly expressed in fibrotic liver tissues and promoted extracellular matrix secretion by HSCs. Given the crucial role of iron accumulation and ROS production in
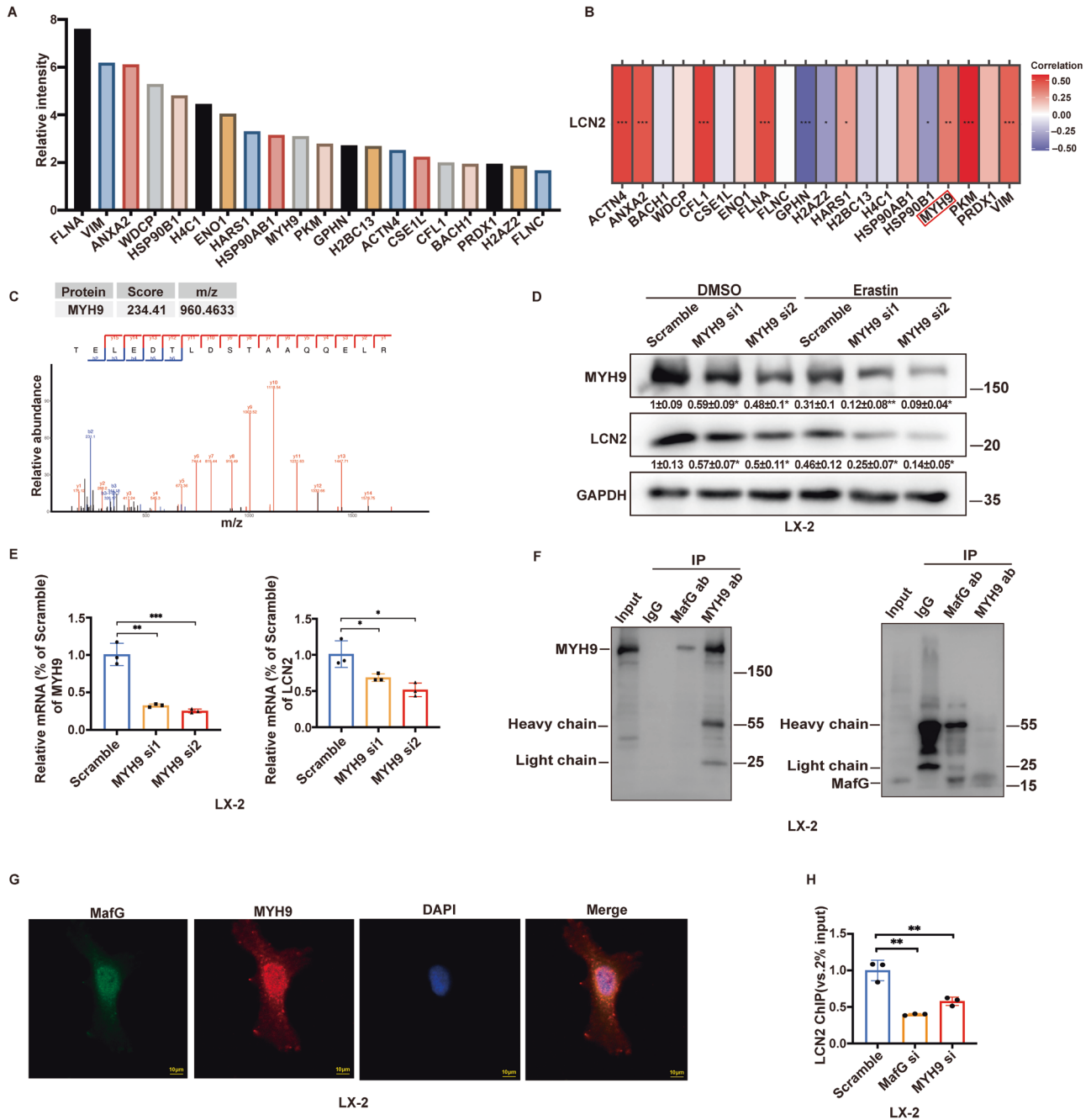
Fig. 6 MYH9 is required for MafG in transcriptional regulation of LCN2. A Relative intensity of top 20 proteins identified in MafG immunoprecipitation mass spectrum. **B** Correlation between LCN2 and top 20 of MafG interacting proteins by bioinformatic analysis. **C** Secondary mass spectrum of MYH9. **D–E** Western blot (**D**) and real-time PCR (**E**) for MYH9 and LCN2 in LX-2 cells treated with vehicle (0.01% dimethyl sulfoxide) or erastin (10 μM) for 24 h following transfection with scramble siRNA and siRNA targeting MYH9 (MYH9 si). **F** Co-immunoprecipitation analysis. Cell extracts were immunoprecipitated with MafG, MYH9 and control (IgG) antibody and immunoblotted with MYH9 and MafG antibody. **G** Representative fluorescent photographs of immunofluorescence analysis for MafG (green) or MYH9 (red) in LX-2 cells. Scale bar, 10μm. **H** ChIP analysis detecting binding of MafG to the LCN2 promoter in control, MafG knockdown and MYH9 knockdown LX-2 cells. Data were represented by the mean ± SEM with corresponded significance. *$P < 0.05$, **$P < 0.01$, ***$P < 0.001$, ns: not significant. The results were repeated in three independent experiments with three replicate each.

ferroptosis, MafG has been proved to participate ferroptosis by influencing iron metabolism and oxidative stress [27, 51, 52]. MafG could bind to the *Hmox1* and *Nqo1* that were ROS associated genes and *transferrin* in ferroptotic response of cisplatin-induced kidney injury [52]. MafG inhibited ferroptosis in bladder urothelial carcinoma through MafG-AS1/PCBP2 mediated upregulation of ferroportin 1, an iron export protein [51]. In addition, MafG heterodimerizes with Nrf2 and transactivates genes involved in

antioxidative signaling pathway [21]. Ferroptosis activator increased interaction between MafG and Nrf2 and enhanced the expression of antioxidants (NQO1 and HO1) in liver cancer [27], whereas the direct bind of Nrf2/MafG to NQO1 and HO1 were not verified. Our study elucidated that MafG interacted with MYH9 to directly bind to LCN2 promoter and regulate HSCs ferroptosis, which further complemented the mechanism regarding MafG-affected iron metabolism in ferroptosis. We also
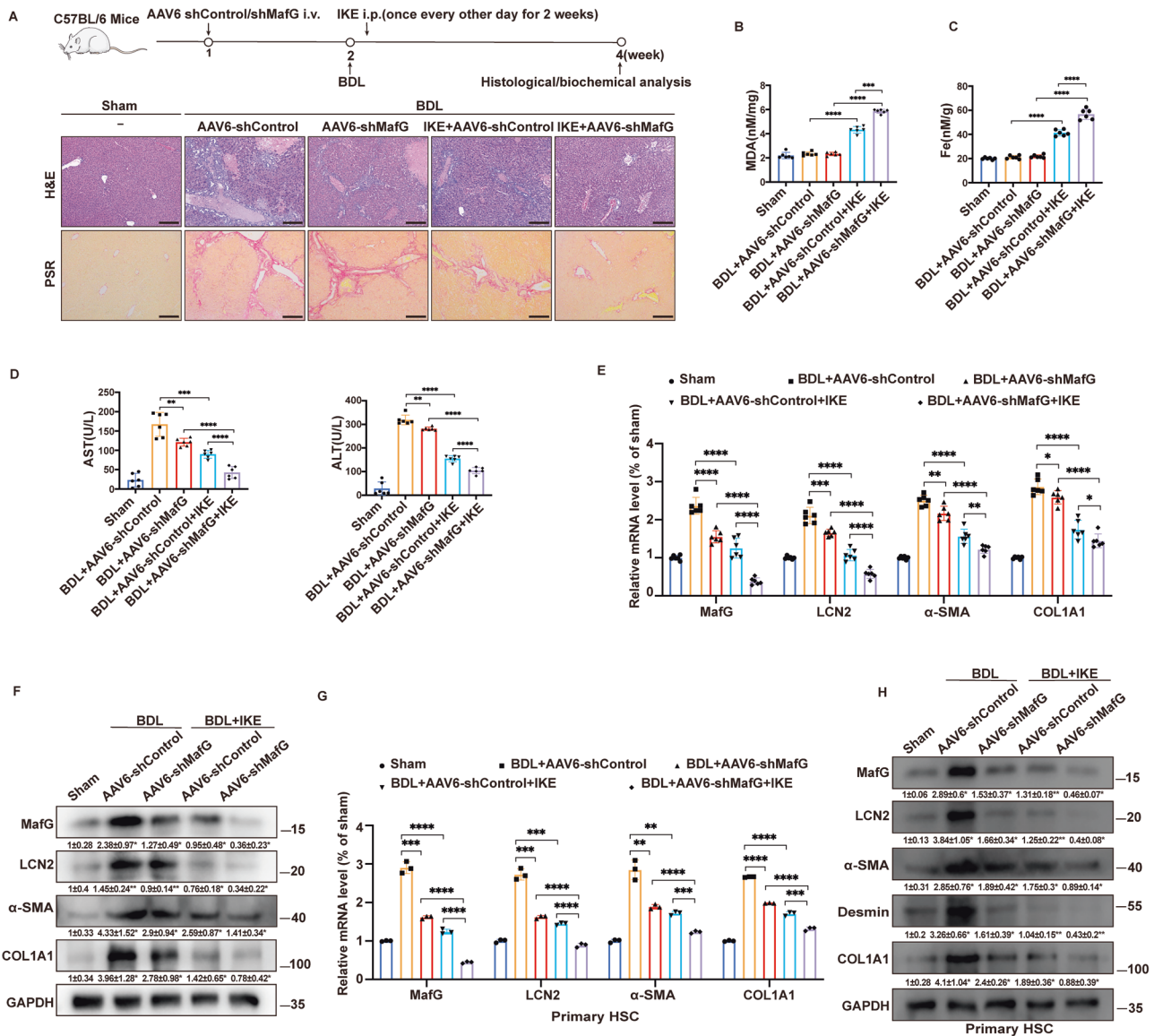
Fig. 7 Block of MafG contributes to the IKE-induced HSC ferroptosis in vivo. A Schematic overview of the animal experimental design and representative photographs of H&E staining, PSR staining in murine hepatic tissues of indicated groups. n = 6/group. Scale bar, 200μm. **B–C** Levels of MDA (**B**) and iron (**C**) in liver tissues of indicated groups after treatment. *n* = 6/group. **D** Serum levels of aspartate aminotransferase (AST) and alanine aminotransferase (ALT) at the time of sacrifice were assayed. *n* = 6/group. **E–F** Levels of MafG, LCN2, α-SMA and COL1A1 in murine liver tissues from indicated groups were examined by real-time PCR (**E**) and Western blot (**F**). Numbers below the blots are densitometric values expressed as ratio of sham. **G** Levels of MafG, LCN2, α-SMA and COL1A1 in primary HSCs from indicated murine liver tissues were detected by real-time PCR. *n* = 3/group. **H** Western blot for MafG, LCN2, α-SMA, Desmin and COL1A1 of primary HSCs from indicated murine liver tissues. Numbers below the blots are densitometric values expressed as ratio of sham. Data were showed by the mean ± SEM with corresponded significance. *$P < 0.05$, **$P < 0.01$, ***$P < 0.001$, ns: not significant. i.v., tail vein injection. i.p., intraperitoneal injection. The results were repeated in three independent experiments with three replicate each.

discovered that blocking Nrf2 had no effect on LCN2 expression level in HSCs. Thus, different target gene and downstream pathway of MafG in ferroptosis may depends on cell type and its various partners. Future researches are required to clarify the relationship between MafG and antioxidants in ferroptosis during liver fibrosis.

Although MYH9 could block sorafenib (a ferroptosis inducer) sensitivity in hepatocellular carcinoma [53] and suppressed cellular ROS levels [54], the function of MYH9 in ferroptosis remains elusive. Our findings revealed that MYH9 is involved in ferroptosis through acting as the partner of MafG. Moreover, MYH9, previously considered as a cytoplasmic myosin [55], was now demonstrated to be localized in the nucleus, in which it post-

transcriptionally modulated the stability of p53 in squamous cell carcinoma [56] or induced CTNNB1 transcription in gastric cancer [41]. We showed that MYH9 participated in transcriptional regulation of LCN2 during liver fibrosis, which indicated the nuclear localization of MYH9 in HSCs. Furthermore, recent study has found that MYH9 possessed a DNA binding domain and could bind to the CTNNB1 promoter [41]. Maf proteins containing heterodimers might bind to the half region of their binding sites (Maf-recognition element) in the promoter of target genes [57]. In addition, MYH9 can induce the transcriptional activity of Nrf2 in head and neck cancer [54]. Therefore, whether MYH9 and MafG bind together to the promoter region of LCN2 or just as a cofactor of MafG needs to be further investigated.

LCN2 was first isolated from human neutrophils attached to the iron-loaded bacterial siderophore and it could interfered the obtain of iron [58]. It was also implied that LCN2 participated in the outflow of iron from the intracellular to extracellular space [40, 59]. Recently, silencing LCN2 was proved to induce intracellular iron accumulation, leading to oxidative damage and ferroptosis in pancreatic ductal adenocarcinoma and liver cancer [17, 39]. Moreover, LCN2 gave rise to chemotherapy resistance of colon cancer cell through inhibiting ferroptosis [60]. We observed that blockade of MafG-LCN2 axis substantially induced iron overload mediated lipid peroxidation in HSCs, which established a novel MafG-dependent LCN2 regulatory pathway for ferroptosis.

In conclusion, our research unveils that transcription factor MafG may be potential target for facilitating HSCs ferroptosis in liver fibrosis. The crosstalk between gene transcription program and iron metabolism makes sense for controlling ferroptosis in pathologic process.

DATA AVAILABILITY
All data generated during this study are available within the article and its supplementary information files can be acquired from the corresponding author upon reasonable request. Human MafG ChIP-seq data were obtained from GEO datasets (https://www.ncbi.nlm.nih.gov/geo/query/acc.cgi?acc=GSE92076). RNA-seq data was acquired from GEO dataset (https://www.ncbi.nlm.nih.gov/geo/query/acc.cgi?acc=GSE14323).

REFERENCES
1. Roehlen N, Crouchet E, Baumert TF liver fibrosis: mechanistic concepts and therapeutic perspectives. Cells. 2020;9:875.
2. Aydin MM, Akcali KC. Liver fibrosis. Turk J Gastroenterol. 2018;29:14–21.
3. Kisseleva T, Brenner D. Molecular and cellular mechanisms of liver fibrosis and its regression. Nat Rev Gastroenterol Hepatol. 2021;18:151–66.
4. Campana L, Iredale JP. Regression of Liver Fibrosis. Semin Liver Dis. 2017;37:1–10.
5. Higashi T, Friedman SL, Hoshida Y. Hepatic stellate cells as key target in liver fibrosis. Adv Drug Deliv Rev. 2017;121:27–42.
6. Zhang X, Zeng Y, Zhao L, Xu Q, Miao D, Yu F. Targeting hepatic stellate cell death to reverse hepatic fibrosis. Curr Drug Targets. 2023;24:568–83.
7. Zhang Z, Yao Z, Wang L, Ding H, Shao J, Chen A, et al. Activation of ferritinophagy is required for the RNA-binding protein ELAVL1/HuR to regulate ferroptosis in hepatic stellate cells. Autophagy. 2018;14:2083–103.
8. Wang L, Zhang Z, Li M, Wang F, Jia Y, Zhang F, et al. P53-dependent induction of ferroptosis is required for artemether to alleviate carbon tetrachloride-induced liver fibrosis and hepatic stellate cell activation. IUBMB Life. 2019;71:45–56.
9. Stockwell BR. Ferroptosis turns 10: Emerging mechanisms, physiological functions, and therapeutic applications. Cell. 2022;185:2401–21.
10. Li J, Cao F, Yin HL, Huang ZJ, Lin ZT, Mao N, et al. Ferroptosis: past, present and future. Cell Death Dis. 2020;11:88.
11. Mou Y, Wang J, Wu J, He D, Zhang C, Duan C, et al. Ferroptosis, a new form of cell death: opportunities and challenges in cancer. J Hematol Oncol. 2019;12:34.
12. Tang D, Chen X, Kang R, Kroemer G. Ferroptosis: molecular mechanisms and health implications. Cell Res. 2021;31:107–25.
13. Park E, Chung SW. ROS-mediated autophagy increases intracellular iron levels and ferroptosis by ferritin and transferrin receptor regulation. Cell Death Dis. 2019;10:822.
14. Patel SJ, Frey AG, Palenchar DJ, Achar S, Bullough KZ, Vashisht A, et al. A PCBP1-BolA2 chaperone complex delivers iron for cytosolic [2Fe-2S] cluster assembly. Nat Chem Biol. 2019;15:872–81.
15. Chen X, Li J, Kang R, Klionsky DJ, Tang D. Ferroptosis: machinery and regulation. Autophagy. 2021;17:2054–81.
16. Dai C, Chen X, Li J, Comish P, Kang R, Tang D. Transcription factors in ferroptotic cell death. Cancer Gene Ther. 2020;27:645–56.
17. Liu J, Song X, Kuang F, Zhang Q, Xie Y, Kang R, et al. NUPR1 is a critical repressor of ferroptosis. Nat Commun. 2021;12:647.
18. Kang R, Kroemer G, Tang D. The tumor suppressor protein p53 and the ferroptosis network. Free Radic Biol Med. 2019;133:162–8.
19. Blank V. Small Maf proteins in mammalian gene control: mere dimerization partners or dynamic transcriptional regulators? J Mol Biol. 2008;376:913–25.
20. Deng Y, Lu L, Zhang H, Fu Y, Liu T, Chen Y. The role and regulation of Maf proteins in cancer. Biomark Res. 2023;11:17.
21. Kannan MB, Solovieva V, Blank V. The small MAF transcription factors MAFF, MAFG and MAFK: current knowledge and perspectives. Biochim Biophys Acta. 2012;1823:1841–6.
22. Yang H, Liu T, Wang J, Li TW, Fan W, Peng H, et al. Deregulated methionine adenosyltransferase alpha1, c-Myc, and Maf proteins together promote cholangiocarcinoma growth in mice and humans(double dagger). Hepatology. 2016;64:439–55.
23. Liu, Yang T, Fan H, Tu W, Li TWH J, Wang J, et al. Mechanisms of MAFG Dysregulation in Cholestatic Liver Injury and Development of Liver Cancer. Gastroenterology. 2018;155:557–71.e14.
24. Yu Y, Yan Y, Niu F, Wang Y, Chen X, Su G, et al. Ferroptosis: a cell death connecting oxidative stress, inflammation and cardiovascular diseases. Cell Death Discov. 2021;7:193.
25. Garcia-Guede A, Vera O, Ibanez-de-Caceres I. When oxidative stress meets epigenetics: implications in cancer development. antioxidants. 2020;9:468.
26. Katsuoka F, Motohashi H, Ishii T, Aburatani H, Engel JD, Yamamoto M. Genetic evidence that small maf proteins are essential for the activation of antioxidant response element-dependent genes. Mol Cell Biol. 2005;25:8044–51.
27. Sun X, Ou Z, Chen R, Niu X, Chen D, Kang R, et al. Activation of the p62-Keap1-NRF2 pathway protects against ferroptosis in hepatocellular carcinoma cells. Hepatology. 2016;63:173–84.
28. Yi K, Liu J, Rong Y, Wang C, Tang X, Zhang X, et al. Biological functions and prognostic value of ferroptosis-related genes in bladder cancer. Front Mol Biosci. 2021;8:631152.
29. Mederacke I, Dapito DH, Affo S, Uchinami H, Schwabe RF. High-yield and high-purity isolation of hepatic stellate cells from normal and fibrotic mouse livers. Nat Protoc. 2015;10:305–15.
30. Oses C, Aouadi M. Kupffer cell and hepatocyte isolation from a single mouse liver by gradient centrifugation. Methods Mol Biol. 2020;2164:1–10.
31. Mederacke I, Hsu CC, Troeger JS, Huebener P, Mu X, Dapito DH, et al. Fate tracing reveals hepatic stellate cells as dominant contributors to liver fibrosis independent of its aetiology. Nat Commun. 2013;4:2823.
32. Ramadori G, Saile B. Portal tract fibrogenesis in the liver. Lab Investig. 2004;84:153–9.
33. Sun B, Karin M. NF-kappaB signaling, liver disease and hepatoprotective agents. Oncogene. 2008;27:6228–44.
34. Wang B, Wang Y, Zhang J, Hu C, Jiang J, Li Y, et al. ROS-induced lipid peroxidation modulates cell death outcome: mechanisms behind apoptosis, autophagy, and ferroptosis. Arch Toxicol. 2023;97:1439–51.
35. Marti-Rodrigo A, Alegre F, Moragrega AB, Garcia-Garcia F, Marti-Rodrigo P, Fernandez-Iglesias A, et al. Rilpivirine attenuates liver fibrosis through selective STAT1-mediated apoptosis in hepatic stellate cells. Gut. 2020;69:920–32.
36. Meng D, Li Z, Wang G, Ling L, Wu Y, Zhang C. Carvedilol attenuates liver fibrosis by suppressing autophagy and promoting apoptosis in hepatic stellate cells. Biomed Pharmacother. 2018;108:1617–27.
37. Zhang Z, Guo M, Shen M, Kong D, Zhang F, Shao J, et al. The BRD7-P53-SLC25A28 axis regulates ferroptosis in hepatic stellate cells. Redox Biol. 2020;36:101619.
38. Jolma A, Yan J, Whitington T, Toivonen J, Nitta KR, Rastas P, et al. DNA-binding specificities of human transcription factors. Cell. 2013;152:327–39.
39. Yao F, Deng Y, Zhao Y, Mei Y, Zhang Y, Liu X, et al. A targetable LIFR-NF-kappaB-LCN2 axis controls liver tumorigenesis and vulnerability to ferroptosis. Nat Commun. 2021;12:7333.
40. Xiao X, Yeoh BS, Vijay-Kumar M. Lipocalin 2: an emerging player in iron homeostasis and inflammation. Annu Rev Nutr. 2017;37:103–30.
41. Ye G, Yang Q, Lei X, Zhu X, Li F, He J, et al. Nuclear MYH9-induced CTNNB1 transcription, targeted by staurosporin, promotes gastric cancer cell anoikis resistance and metastasis. Theranostics. 2020;10:7545–60.
42. Zhang Y, Tan H, Daniels JD, Zandkarimi F, Liu H, Brown LM, et al. Imidazole Ketone Erastin Induces Ferroptosis and Slows Tumor Growth in a Mouse Lymphoma Model. Cell Chem Biol. 2019;26:623–33.e9.
43. Zhang Z, Guo M, Li Y, Shen M, Kong D, Shao J, et al. RNA-binding protein ZFP36/TTP protects against ferroptosis by regulating autophagy signaling pathway in hepatic stellate cells. Autophagy. 2020;16:1482–505.
44. Rezvani M, Espanol-Suner R, Malato Y, Dumont L, Grimm AA, Kienle E, et al. In Vivo hepatic reprogramming of myofibroblasts with AAV vectors as a therapeutic strategy for liver fibrosis. Cell Stem Cell. 2016;18:809–16.
45. Lambert SA, Jolma A, Campitelli LF, Das PK, Yin Y, Albu M, et al. The human transcription factors. Cell. 2018;172:650–65.
46. Sun Y, Chen P, Zhai B, Zhang M, Xiang Y, Fang J, et al. The emerging role of ferroptosis in inflammation. Biomed Pharmacother. 2020;127:110108.
47. Sui M, Jiang X, Chen J, Yang H, Zhu Y. Magnesium isoglycyrrhizinate ameliorates liver fibrosis and hepatic stellate cell activation by regulating ferroptosis signaling pathway. Biomed Pharmacother. 2018;106:125–33.
48. Kong Z, Liu R, Cheng Y. Artesunate alleviates liver fibrosis by regulating ferroptosis signaling pathway. Biomed Pharmacother. 2019;109:2043–53.
49. Wang H, An P, Xie E, Wu Q, Fang X, Gao H, et al. Characterization of ferroptosis in murine models of hemochromatosis. Hepatology. 2017;66:449–65.

50. Carino A, Biagioli M, Marchiano S, Fiorucci C, Bordoni M, Roselli R, et al. Opposite effects of the FXR agonist obeticholic acid on Mafg and Nrf2 mediate the development of acute liver injury in rodent models of cholestasis. Biochim Biophys Acta Mol Cell Biol Lipids. 2020;1865:158733.

51. Xiang L, Zeng Q, Liu J, Xiao M, He D, Zhang Q, et al. MAFG-AS1/MAFG positive feedback loop contributes to cisplatin resistance in bladder urothelial carcinoma through antagonistic ferroptosis. Sci Bull. 2021;66:1773–88.

52. Kim DH, Choi HI, Park JS, Kim CS, Bae EH, Ma SK, et al. Farnesoid X receptor protects against cisplatin-induced acute kidney injury by regulating the transcription of ferroptosis-related genes. Redox Biol. 2022;54:102382.

53. Lin X, Li AM, Li YH, Luo RC, Zou YJ, Liu YY, et al. Silencing MYH9 blocks HBx-induced GSK3beta ubiquitination and degradation to inhibit tumor stemness in hepatocellular carcinoma. Signal Transduct Target Ther. 2020;5:13.

54. You GR, Chang JT, Li YL, Huang CW, Tsai YL, Fan KH, et al. MYH9 Facilitates Cell invasion and radioresistance in head and neck cancer via modulation of cellular ROS levels by activating the MAPK-Nrf2-GCLC pathway. Cells. 2022;11:2855.

55. Pecci A, Ma X, Savoia A, Adelstein RS. MYH9: structure, functions and role of non-muscle myosin IIA in human disease. Gene. 2018;664:152–67.

56. Schramek D, Sendoel A, Segal JP, Beronja S, Heller E, Oristian D, et al. Direct in vivo RNAi screen unveils myosin IIa as a tumor suppressor of squamous cell carcinomas. Science. 2014;343:309–13.

57. Eychene A, Rocques N, Pouponnot C. A new MAFia in cancer. Nat Rev Cancer. 2008;8:683–93.

58. Goetz DH, Holmes MA, Borregaard N, Bluhm ME, Raymond KN, Strong RK. The neutrophil lipocalin NGAL is a bacteriostatic agent that interferes with siderophore-mediated iron acquisition. Mol Cell. 2002;10:1033–43.

59. Flo TH, Smith KD, Sato S, Rodriguez DJ, Holmes MA, Strong RK, et al. Lipocalin 2 mediates an innate immune response to bacterial infection by sequestrating iron. Nature. 2004;432:917–21.

60. Chaudhary N, Choudhary BS, Shah SG, Khapare N, Dwivedi N, Gaikwad A, et al. Lipocalin 2 expression promotes tumor progression and therapy resistance by inhibiting ferroptosis in colorectal cancer. Int J Cancer. 2021;149:1495–511.

AUTHOR CONTRIBUTIONS
Conceptualization, YC and TL; Methodology, YD, LL; Software, DZ and HZ; Validation, YD, LL, YT. and XT; Formal analysis, YF and MG; Investigation, HY and BY; Resources, YC; Data curation, YD and YC; Writing – Original Draft Preparation, YD: Writing – Review & Editing, YC and TL; Visualization, YD; Supervision, YC and TL; Project Administration, YC and TL. All authors have read and approved the final version of the manuscript.

COMPETING INTERESTS
The authors declare no competing interests.

ETHICS APPROVAL
All experimental procedures for mice were carried out under the Central South University Animal Care and Use Committee criteria. The research protocol for human liver samples conformed to the guidelines of ethical committees of the Xiangya Hospital of Central South University.

ADDITIONAL INFORMATION
Supplementary information The online version contains supplementary material available at https://doi.org/10.1038/s41418-024-01322-5.

Correspondence and requests for materials should be addressed to Ting Liu or Yongheng Chen.

Reprints and permission information is available at http://www.nature.com/reprints

Publisher's note Springer Nature remains neutral with regard to jurisdictional claims in published maps and institutional affiliations.